PERGAMON

International Journal of Solids and Structures 36 (1999) 2773–2788

INTERNATIONAL JOURNAL OF SOLIDS and STRUCTURES

Spherical impression of thin elastic films on elastic–plastic substrates

Matthew R. Begley, Anthony G. Evans, John W. Hutchinson*

Division of Engineering and Applied Sciences, Harvard University, Cambridge, MA 02138, U.S.A.

Received 29 September 1997; in revised form 2 April 1998

Abstract

The mechanical behavior of thin elastic films deposited onto structural alloys plays a critical role in determining film durability. This paper presents analysis of an impression experiment designed to evaluate some of the relevant properties of these films. The modeling provides quantitative strain information which can be used to estimate the fracture toughness of the film, the static friction coefficient of the surface and the constitutive behavior of the substrate. Results are presented for radial and circumferential strain distributions in the film relevant to the interpretation of cracking patterns. Additionally, load-displacement curves are provided that may be used to evaluate the plastic properties of the substrate. To facilitate estimates of the film cracking strain through correlation with experiments, the radial strain distributions are presented as functions of impression depth, yield strain and hardening exponent.

1. Introduction

There is an increasing awareness that surface functionality can be achieved in conjunction with thermomechanical integrity by depositing thin films onto structural alloys. The films enhance the abrasion or corrosion resistance of the system and the lubricity of the surface. Typical systems include nitrides, diamond and diamond-like carbon (DLC) (Bull and Chaiken, 1995; Wei et al., 1992; Blanpain et al., 1993; Bull, 1995; Deng and Brown, 1995; Meletis et al., 1995; Grill et al., 1993; Grill and Patel, 1993; Bentzon et al., 1995). Performance issues concerned with adhesion are addressed by using thin interlayers of Cr or Ti (Bentzon et al., 1995). These interlayers increase the interface fracture toughness to levels that exceed the toughness of the coating. Consequently, film cracking becomes the performance limiting mechanical response. However, the interface may still be susceptible to either stress corrosion or cyclic crack growth and fatigue failure. Test methods that probe the cohesion of thin films and the cyclic properties of the interface in a straightforward

* Corresponding author. Tel.: 001 617 495 2848; E-mail: hutchinson@husm.harvard.edu

0020–7683/99/$ - see front matter
PII: S0020–7683(98)00128–0

manner are needed to develop a life prediction approach. This article presents analyses of a sphere impression test (Wang et al., 1997; Weppelmann and Swain, 1996) which has the attributes of being quite simple and amenable to quantification.

In order to motivate the results presented in this paper, the test is briefly described. Experimental results are presented in a companion paper (Wang et al., 1998). A small hard sphere ~ 1 mm in diameter, D, made from tungsten carbide or silicon nitride, is pushed into the surface, while the load, P, and the depth of the impression, δ, are continuously measured. Relative impression depths, δ/D, in the order of 0.1 are used to ensure extensive plastic straining in the substrate. After removal of the sphere, the impression is examined either in the optical or scanning electron microscope. Such observations reveal patterns of cracks in the film caused by tensile stretching in the impressed region (Wang et al., 1998) (Fig. 1). The cracks are typically circumferential and located near the perimeter of the impression. In some cases, smaller radial cracks occur both inside and outside the impression. In other cases, regions of the film within the cracked zone spall from the substrate.

The primary goal in modeling the test is to determine the strain in the thin film as a function of impression depth. The cracking strain in the film can then be determined by comparison with experiments, whereupon the crack spacing and orientation (i.e. radial or circumferential) may be used to corroborate the modeling, and vice versa. Typically, the film is very thin compared with the size of the sphere used to make the impression; in Fig. 1, the ratio of film thickness to ball diameter, $t:D$ is approximately 0.05. As such, the film does not play a significant role in the indentation process. The strain in the film is governed by the surface strain in the substrate. Consequently, the experiment is modeled by ignoring the influence of the film on the indentation, except through its effects on the friction coefficient, and simply analyzing the elasto-plastic substrate material. Should the surface profile of the impression develop sharp corners, the extra bending strains that arise in the elastic film can be estimated by calculating the curvature of the indented surface.

There is substantial literature on modeling spherical (or Brinell) indentation (e.g. Johnson, 1986; Biwa and Storåkers, 1995; Hill et al., 1993) including efforts that directly model the elastic layer (Kral et al., 1993, 1994a, 1994b; Komvopoulos, 1989; Weppelmann and Swain, 1996). Investigations into the effect of film thickness and compliance have focused on indentation depths on the order of the film thickness (or smaller) and film moduli twice that of the substrate (or greater). The focus here is on much thinner films, where thickness and compliance effects are significantly diminished. The large indentation depths of interest (relative to the film thickness) require flow theory to accurately describe plastic deformation; previous analyses using deformation

Fig. 1. Experimental cracking patterns in diamond-like carbon (DLC) on high strength steel. Each pattern is a scanning electron microscope image looking down on a 1 μm thick DLC film deposited onto a rough steel surface. The images have been taken after plastic straining in the horizontal direction, beyond the threshold strain for cracking (2.1%). The micron markers on each illustrate the magnification. In all cases, the cracks in the DLC are vertical, while the horizontal features are grooves in the original steel surface, topographically reproduced on the surface of the DLC film. (a) A high magnification view of the DLC illustrating the residual crack opening displacements. (b) A lower magnification view showing the steel substrate (top) and the DLC with multiple cracks (bottom). Note that the cracks extend fully across the DLC. (c) The same region as (b) imaged to obtain a different contrast between the substrate, identified as FeCrC(Ni) and the DLC, denoted WC.

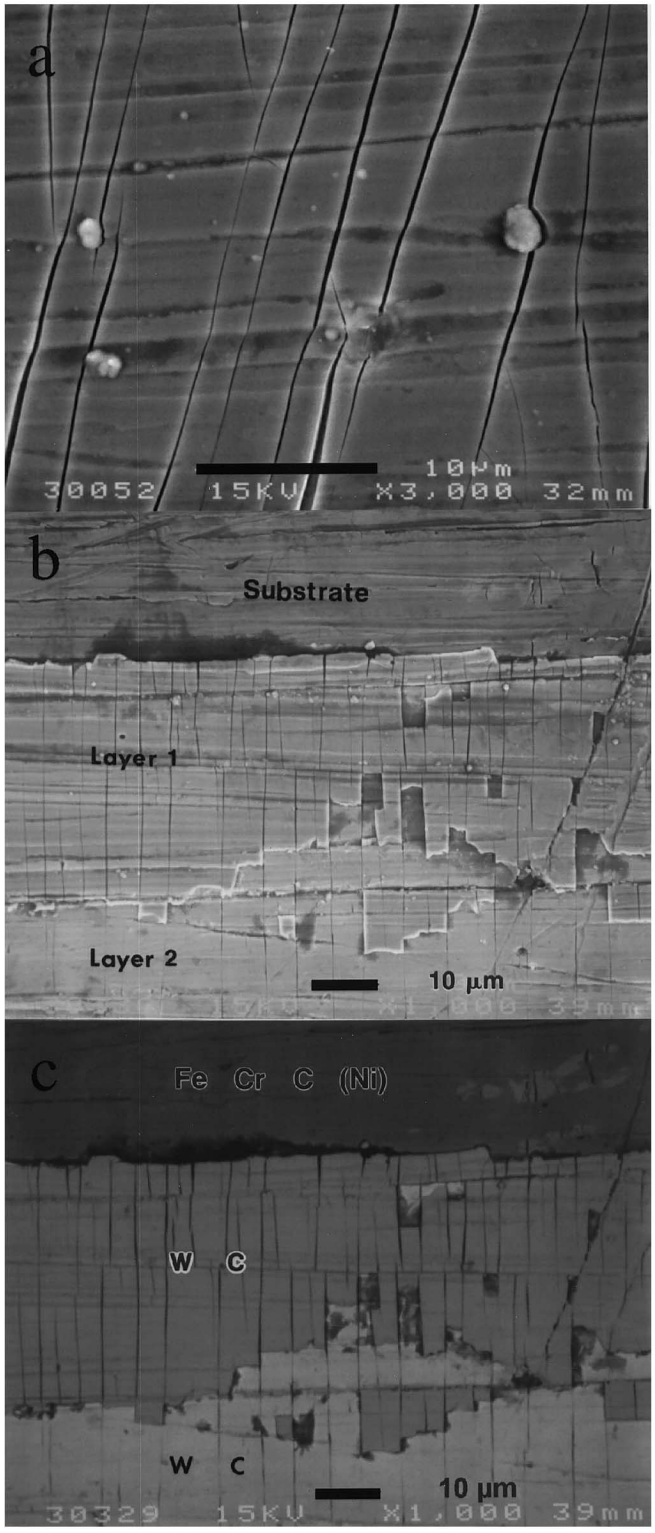
a
10μm
30052 15KV X3,000 32mm
b
Substrate
Layer 1
Layer 2
10 μm
c
Fe Cr C (Ni)
W C
W C
10 μm
30329 15KV X1,000 39mm

theory are inappropriate, although indentation depths as a function of load may be similar. The transition to the regime where film thickness has relatively little effect has not been analysed in detail. Preliminary simulations† imply that it applies when the modulus of the film is equal to or smaller than that of the substrate, and the depth of indentation is greater than about five times the thickness of the film.

Finally, previous efforts have focused on the resulting stress states, predicted hardness, and Mises contours of stress and strain (e.g. Johnson, 1986; Biwa and Storåkers, 1995; Hill et al., 1993; Kral et al., 1993, 1995a, 1995b; Storåkers et al., 1997). A notable exception is the work of Biwa and Storåkers (1995), who made use of a similarity transform to calculate strain distributions for a variety of indenter geometries. Their results are very detailed; however, extracting quantitative information from their results is difficult, and for some cases, not possible. These previous efforts were used to benchmark the modeling presented here and provide quantitative information regarding the numerical accuracy of our results.

2. Constitutive behavior and finite element model

Before proceeding, it should be first noted that significant differences in strain response have been found upon using the flow and deformation theories of plasticity. Previous analyses have illustrated that both theories predict nearly identical load-displacement histories during loading (Hill et al., 1989; Johnson, 1970, 1985). However, the strain distributions are found to be very different and may disagree by more than a factor of two. That the two analyses coincide for load-displacement curves, but disagree for strain distributions can be explained as follows. The indentation load during deformation is primarily governed by a large hemi-spherical volume around the impression which undergoes nearly proportional loading. The two theories coincide for this case. However, the loading on the material directly underneath the indenter and near the surface is non-proportional. That is, the material at the center of the impression is in compression in the elastic range and in tension in the plastic range, as material flows out from underneath the indenter. To accurately capture these strain reversals, deformation theory is inappropriate. Flow theory, finite strain and large displacement are necessary features of the modeling. This has caused inaccuracies in previous strain analyses based on deformation theory (Weppelman and Swain, 1996).

Accordingly, the substrate has been modeled using J_2 plasticity flow theory with isotropic hardening and a Ramberg–Osgood stress-strain law. The effective stress–strain relationship was chosen so that in uniaxial tension the behavior of the substrate follows the Ramberg–Osgood relation

$$\varepsilon = \frac{\sigma}{E} + \alpha \frac{\sigma_y}{E}\left(\frac{\sigma}{\sigma_y}\right)^n \tag{1}$$

where E is the Young's modulus, σ_y is the yield stress, n is the strain hardening exponent and α is

† M.R. Begley and M.A. Jakubowski, work in progress.

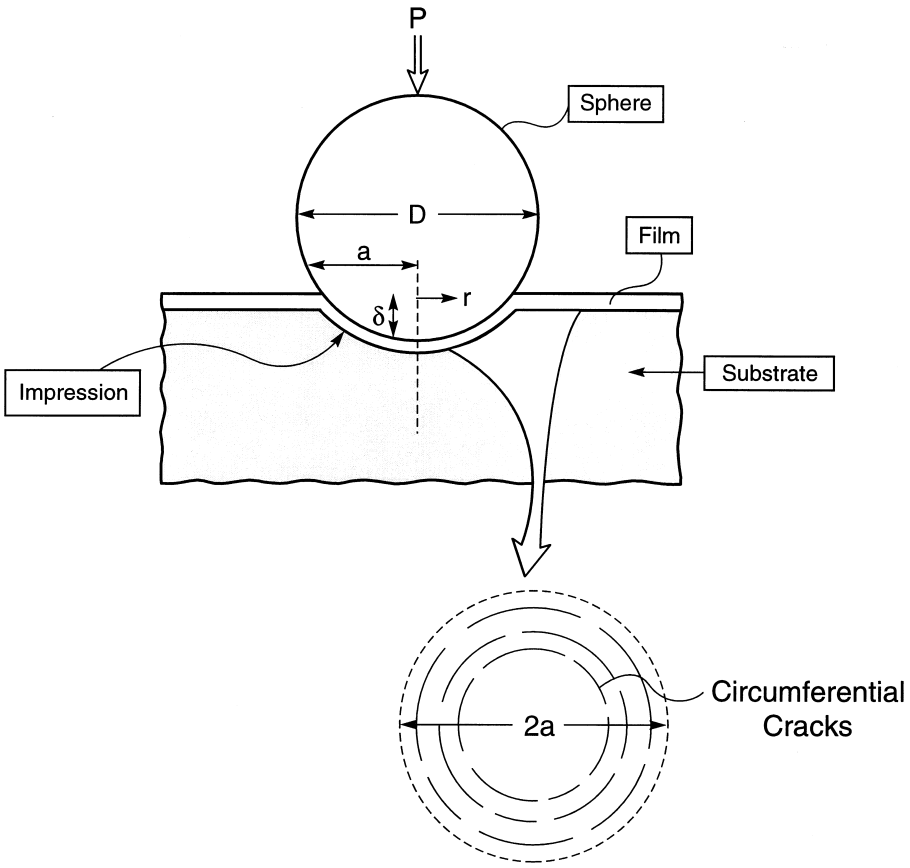

Fig. 2. Schematic of the indentation model.

a fitting coefficient which controls the onset of non-linearity. For simplicity, α was taken to be 0.03 for all cases, as this value provided an exact fit for the experimental data collected for a high-strength, low strain hardening steel. Results are presented for two strain hardening coefficients ($n = 10$ and 25), with three yield strains ($\varepsilon_y = \sigma_y/E = 1/80$, $1/200$ and $1/240$), that encompass the range for steels, as well as aluminum and nickel alloys.

A schematic of the indentation model is given in Fig. 2. The spherical indenter was assumed to be rigid. Finite strain and large displacement analysis were used to model the substrate. The finite element modeling utilized the commercial code ABAQUS. A constant coefficient of friction, μ, was assumed, relating the normal traction at the interface (t_n) to the tangential traction (t_s) via, $t_s = \mu t_n$. The problem was solved using the contact algorithms available in this code; friction between the sphere and substrate is accounted for using a Lagrange multiplier method to apply the constraint between t_s and t_n. Eight-noded axisymmetric elements were used, with approximately 35 elements in the contact zone. Convergence studies revealed that this mesh, though coarser than some previous efforts, was adequate for capturing the strain profiles near the surface of the substrate. The mesh dependence was very localized near the edge of contact and did not affect the

strain distributions in the areas of interest. Since convergence difficulties and element locking did not appear to be a problem, results are presented for standard 3×3 Gaussian integration.

3. Impression mechanics

Load-displacement histories for spherical indentations have been well documented (e.g. Kral et al., 1993, 1995a, 1995b) and show the same general characteristics as the experiments. A direct connection between the load-displacement history and the tensile stress-strain behavior of the material may be made by plotting the hardness, or indentation stress ($H = P/\pi a^2$), normalized by the yield strength, as a function of contact radius, a, normalized in accordance with the effective indentation strain, $\varepsilon_I = (E/\sigma_y)(a/D)$. This connection is clearest during fully plastic indentation, where the plastic zone envelops the contact region (Hill et al., 1989, Biwa and Storåkers, 1995). In this limit, the stress/strain behavior of the material is accurately captured by,

$$\sigma = \sigma_y \left(\frac{1}{\alpha \varepsilon_y} \right)^{1/n} \varepsilon^{1/n} \tag{2}$$

resulting in the following relationship between hardness and contact size (Tabor, 1951),

$$\frac{H}{\sigma_y} = \phi \left(\frac{1}{\alpha} \frac{\beta}{\varepsilon_y} \frac{a}{D} \right)^{1/n} \tag{3}$$

where ϕ and β are constants. Tabor's experimental results for pure power-law materials imply $\phi \approx 2.8$ and $\beta \approx 0.4$, while corresponding numerical results from Biwa and Storåkers (1995) are: 3.07 and 0.32, respectively.

The transition to this fully plastic limit occurs at large contact radii, when $\varepsilon_I > 50$ (Johnson, 1970). At the smaller strains relevant to the spherical impression tests being modeled, the analogous measures of indentation stress/strain have not been explicitly defined. Here it is postulated that the same normalizations apply, even at small ε_I, where elasticity effects are dominant. The present calculations plotted in accordance with this assertion (Fig. 3) substantiate that this relationship is, indeed, independent of the yield strain and the elastic properties of the substrate, and only a function of the hardening exponent. There is a small effect of α, which has been neglected‡. Note that the indentation stresses are appreciably smaller than those expected for the fully plastic limit eqn (3), over most of the range. Only when $n = 25$ is this limit approached at large a.

From an experimental point of view, the indentation load and displacement are the easiest quantities to measure during the indentation process. As such, it is desirable to find the relationship between the indentation depth δ and the contact size a. This relationship must be a function of the material properties, because smaller yield strains and higher hardening exponents generally imply larger amounts of material flow, and hence, larger contact sizes. However, for the material properties considered here, this effect is found to be insignificant, because material flow from under the indenter is negligible. As a result, the contact radius can be well-approximated by the circle

‡ Increasing α by an order of magnitude decreased the hardness by about 15%.

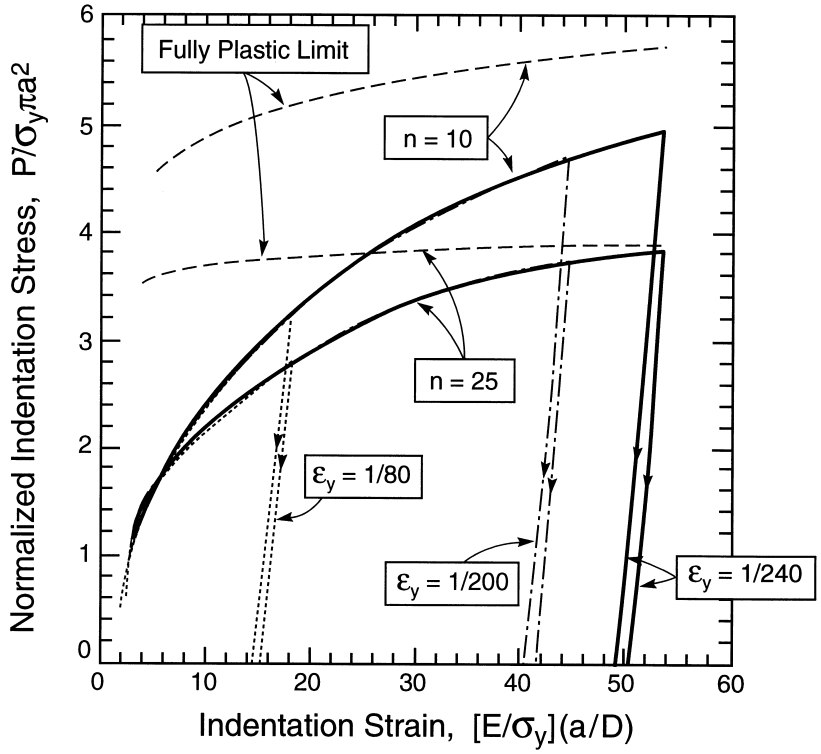

Fig. 3. Normalized indentation stress as a function of indentation strain calculated for two values of hardening exponent and three yield strains. Also shown are the fully plastic curves (3).

where the sphere crosses the plane of the undeformed material. The contact radius is then governed (for $\delta/D \ll 1$) by,

$$\frac{a}{D} = \sqrt{\frac{\delta}{D}} \tag{4}$$

Note that this relationship differs from the classical Hertzian relationship by a factor of $\sqrt{2}$; for strictly elastic results, eqn (4) is inappropriate. However, surprisingly small amounts of plasticity are enough to change the contact radius. This is a very useful result, since the edge of contact can be estimated directly from the displacement of the indenter, without concerns about either unloading effects or details of the contact. It is interesting to note that eqn (4) is a good approximation for the range of indentation sizes presented here ($0 \leqslant a/D \leqslant 0.3$), regardless of the piling-up or sinking-in of material around the indenter.

Finally, the load upon initial unloading is found from a Hertzian analysis for a sphere within a spherical cavity having the same diameter (created upon loading). The contract size remains constant during initial unloading, and the pressure/displacement relationship is well approximated by that for a flat indenter having radius equal to the initial contact size. Using eqn (4), the initial

unloading portion of the curve is thus approximated by (e.g. Briscoe et al., 1994; Pharr et al., 1992);

$$P = \frac{4}{\pi(1-v^2)} ED^2 \left(\frac{\delta}{D}\right)^{3/2} \tag{5}$$

Deviations from eqn (5) occur only at small values of pressure, when the changing contact size begins to play a significant role. This relation may be used to calibrate the compliance of the loading system.

4. Strain profiles

The primary goal of the modeling is to determine the strains at the surface. The radial strain, $\varepsilon_{rr}(r, 0)$, is shown in Fig. 4 for several values of the friction coefficient. It is readily apparent that friction between the indenter and the surface has a major effect on the strain distribution, which has not been realized in previous analyses. As the friction coefficient increases between 0 and about 0.3, the location of maximum tensile strain transitions from the center of the impression towards

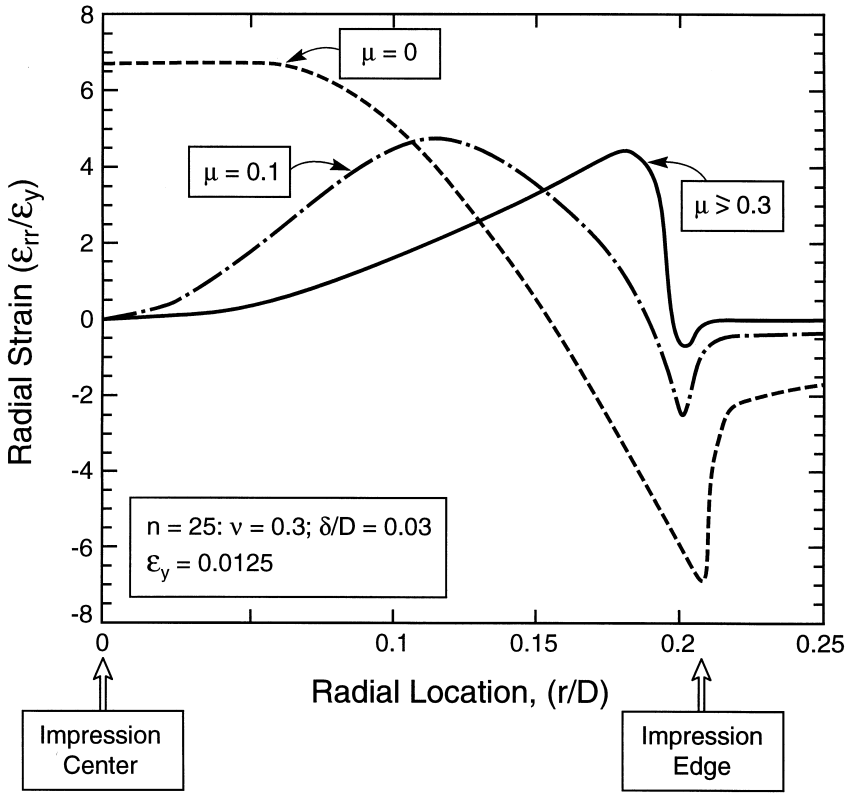

Fig. 4. Radial strain as a function of distance from the center of the impression for various friction coefficients.

the edge of contact. Note that this edge occurs just inside the large negative spike in the radial strain curve. Most importantly, for values of $\mu \geqslant 0.3$, slip is prevented (except for an insignificant region near the edge of contact) and the results become indistinguishable from that for sticking contact. That is, the strain profiles are independent of μ for values approximately greater than one third. In such cases, the friction between the sphere and surface severely limits the magnitude of the strain because material is unable to flow out from under the center of the contact area. These findings for large μ (Fig. 4) are consistent with the experimental film cracking results (Wang et al., 1998) (Fig. 1), since both imply large radial strains near the edge of contact.

In order to accomplish the objective of being able to predict cracking strains in the film, strain profiles (such as those in Fig. 4) must be examined for a variety of impression depths and material properties. For films of primary interest, the friction coefficient exceeds 0.3, indicating that sticking friction is an appropriate choice. Since the tensile radial strains dominate inside the contact area and experiments indicate that this is the strain component governing cracking, further emphasis is on these strains. Results have been compiled for the three yield strains and two hardening exponents, noted above.

The radial strain distributions (Fig. 5a–c) obtained for three impression depths ($\delta/D = 0.017$, 0.033 and 0.05) reveal that, as the impression depth increases, the maximum tensile strain along the surface near the edge of contact increases. Moreover, after a significant portion of the material under the indenter has yielded, the strain profiles begin to develop in a self-similar manner. This condition arises because, once the material is drawn under the indenter, it is locked in place by friction and all of the subsequent straining occurs outside the area of contact. As the indentation depth increases, the fully plastic solution is approached, which is completely self-similar (Biwa and Storåkers, 1995). This effect can be seen in Fig. 3, where the indentation load approaches that of the self-similar solution, and in Fig. 5a–c, where the strain profiles develop with the same spatial dependence. This is an attractive and very useful feature, since strain distributions for deeper impressions can be extrapolated from the results shown in Fig. 5. Only at the large yield strains, $\varepsilon_y = 1/80$ (Fig. 5a), are the elastic strains significant, whereupon greater depths are required to reach a self-similar strain distribution. This is evident in the small difference in the radial strain distributions for $\delta/D = 0.03$ and 0.05. For completeness, the hoop strain distributions near the surface are given in Fig. 6. The magnitudes are tensile, but significantly smaller than the radial component.

The radial strain distributions can be used in conjunction with experiments to estimate the cracking strain in the film (Wang et al., 1998). To facilitate this, functions were fit to the results in Fig. 5. Since the region of interest is the increasing portion of the strain profiles, the self-similar feature of the indentation process makes this relatively simple. That is, a single function can be used to express the radial strain for all indent depths. The cut-off is the location of maximum strain at the contact radius, which can be found as a function of indent depth using eqn (4). The radial strain distributions when $r \leqslant a$ are found to be well-represented by

$$\frac{\varepsilon_{rr}}{\varepsilon_y} = m_1(\varepsilon_y)\left(\frac{r}{D}\right) + m_2(\varepsilon_y, n)\left(\frac{r}{D}\right)^3, \tag{6a}$$

where

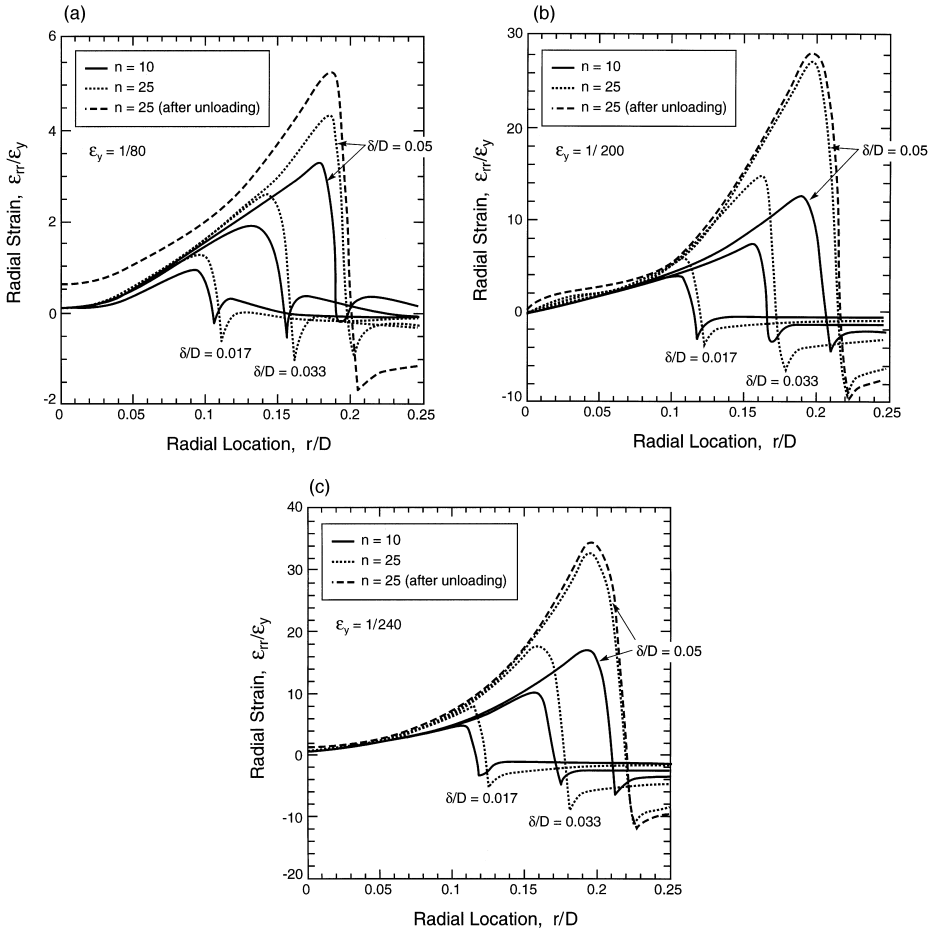

Fig. 5. Radial strain profiles at three indent depths for $\mu \geqslant 0.3$. The lines with long dashes are the strains after complete unloading ($n = 10$ and 25). (a) $\varepsilon_y = 0.0125$, (b) $\varepsilon_y = 0.005$, (c) $\varepsilon_y = 0.0042$.

$$m_1(\varepsilon_y) = 1.45 + \frac{0.14}{\varepsilon_y}, \tag{6b}$$

and

$$m_2(\varepsilon_y, n) = [1466 - 118n] + [-22.7 + 1.8n]\left(\frac{1}{\varepsilon_y}\right) + [0.075 - 0.003n]\left(\frac{1}{\varepsilon_y}\right)^2. \tag{6c}$$

The functions representing the numerical results are excellent fits for any $r/D > 0.05$, and for all yield strains or hardening exponents in the ranges: $10 \leqslant n \leqslant 25$ and $0.00417 \leqslant \varepsilon_y \leqslant 0.0125$. Since small r/D values are not of interest, the fit given by eqns (6a–c) covers the range of interest for most alloys. The functions are valid for indentation strains $\varepsilon_I > 6$ or so, and $\leqslant 60$, although the upper limit is probably considerably higher based on the smoothness of the fits.

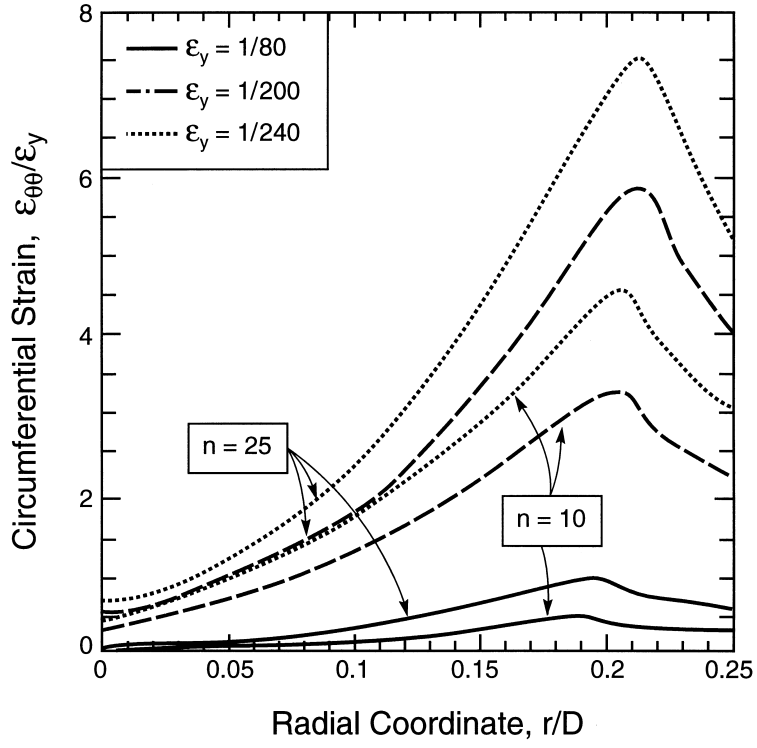

Fig. 6. Circumferential strain profiles at $\delta/D = 0.05$.

Note that the normalization of the strain ε_{rr} by the yield strain ε_y does not provide universality (Fig. 5). Instead, decreasing the yield strain increases the plastic strain (though not necessarily the total strain) and, moreover, larger strains arise for smaller levels of strain hardening. It is apparent from Fig. 5 and from eqn (6) that normalizing through the product $\varepsilon_{rr} \cdot \varepsilon_y$ more successfully consolidates the results. This can be ascertained upon multiplying eqns (6a–c) by ε_y^2. While the reasons for this scaling are not yet understood, the following features might be responsible: (i) The near surface strains ε_{rr} increase proportionally with a/R_p, where R_p is the plastic zone size. (ii) At specified contact radius, the plastic zone size becomes larger as the yield strain ε_y increases, because the loads needed to form the impression increase. Accordingly, if this scaling has the explicit form, $R_p/a \sim \varepsilon_y$, then the product $\varepsilon_{rr} \cdot \varepsilon_y$ becomes the relevant entity scaling the surface strains.

5. Surface profiles

The static friction at the contact can be estimated from the surface profiles after unloading (Fig. 7). Two characteristics are prominent: (i) the elastic recovery results in shallowing of the impression, and (ii) the pile-up around the edge of contact is a strong function of the friction coefficient. The latter arises because even small amounts of friction inhibit material from flowing out. The pile-up as a function of friction coefficient is plotted on Fig. 8, for $n = 25$ and $\varepsilon_y = 0.0125$. A fit to the

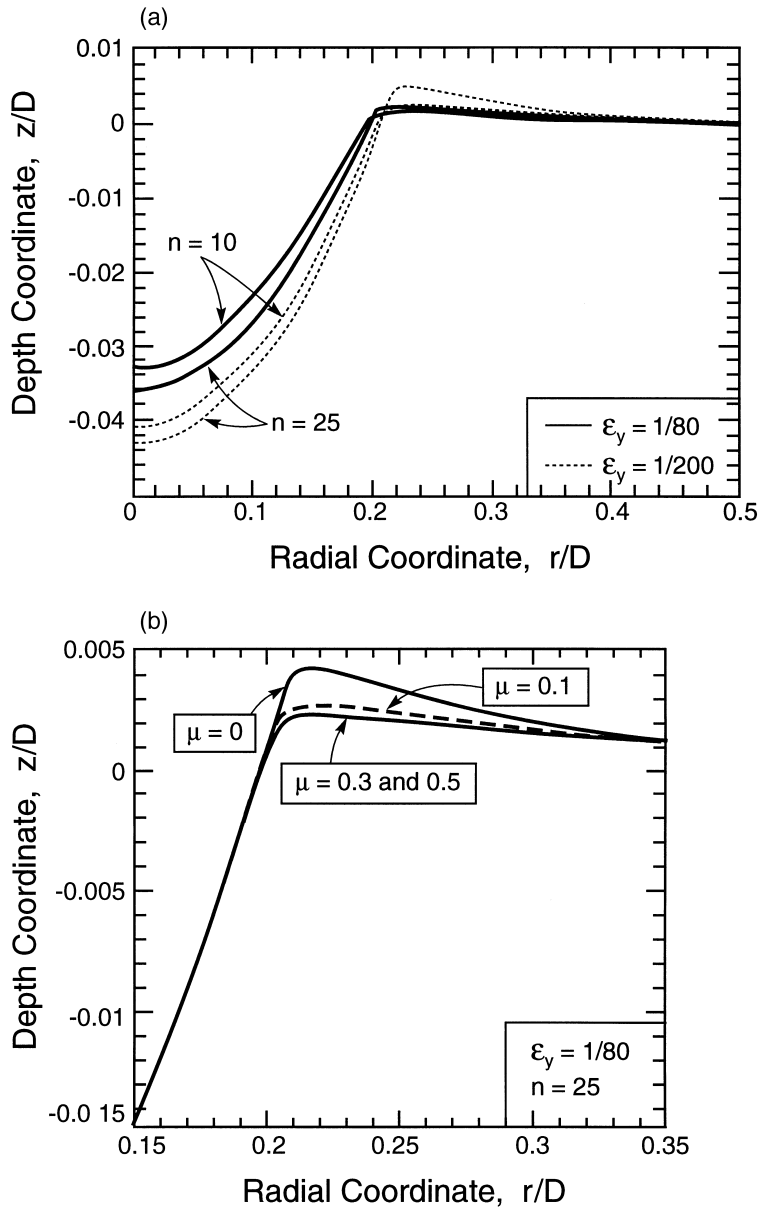

Fig. 7. Deformed surface profiles after unloading, (a) for various material properties, (b) for various friction coefficients.

height of the deformed surface, h, is given by,

$$\frac{h}{D} = H_0 - H_{0.5} \exp\left(- \frac{0.02}{(0.002+\mu)^{1.3}} - 0.21\mu \right) \tag{7}$$

where H_0 and $H_{0.5}$ represent h/D when $\mu = 0$ and 0.5, respectively.

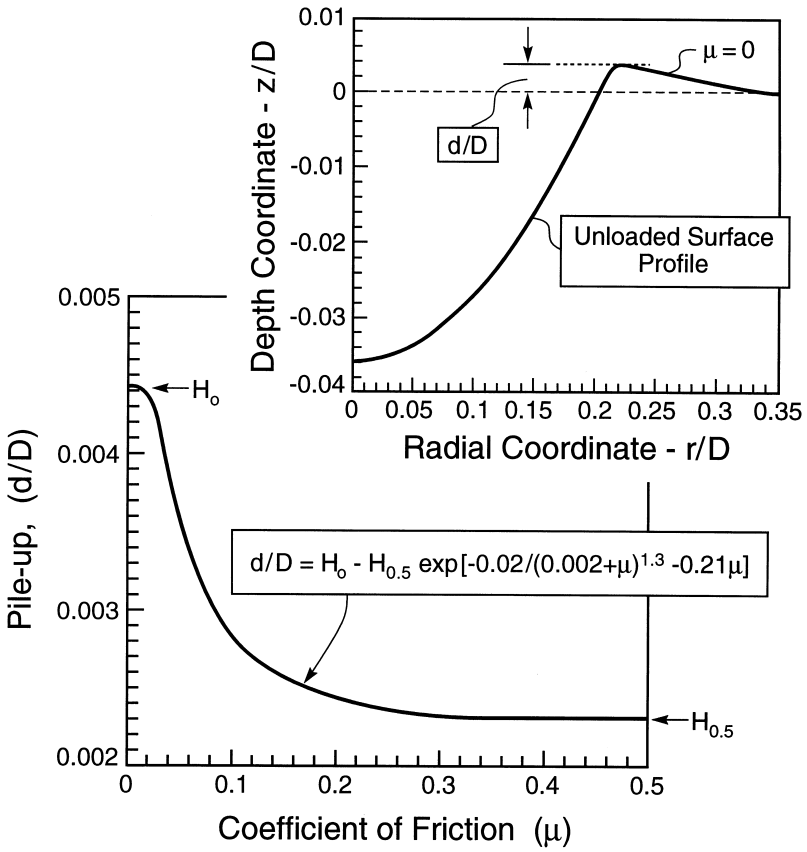

Fig. 8. Pile-up (defined as the maximum height of the deformed surface above the plane of undeformed material) as a function of friction coefficient.

This formula can be used to estimate μ from h/D measurements when the film is very thin compared to the ball diameter and depth of indentation. The absolute size of the pile-up does not present a problem since modern profilometry (such as AFM) allows accurate determination of very small displacements. Naturally, the pile-up is a strong function of the film thickness (thicker films inhibit pile-up) and elastic properties; the results presented here are only valid for very thin films ($t/D \leqslant 25$) and deeper indents ($\delta/t \geqslant 5$), where the film has a minimal effect on the displacement profile.

6. Concluding remarks

The present analysis has for the first time determined the near surface plastic strains that occur beneath a sphere impressed into a surface. For this purpose, it has been necessary to use the flow theory of plasticity, because of the non-proportional loading that occurs in this region. It has been shown that these strains are strongly influenced by the static friction coefficient, μ, with a complete

change in the spatial dependence occurring as the friction coefficient changes from 0 to 0.3. Above 0.3 there are no further changes in the strain field with increase in μ, because thereafter, sticking occurs whenever each point on the surface is drawn beneath the indenter. In this range, the radial tensile strains are larger than the circumferential strains and exhibit a maximum near the periphery of the contact. These strains have been characterized for a range of yield strains, elastic properties and strain hardening exponents representative of structural alloys.

The radial strains are the basis for interpreting the cracking and debonding behavior of thin elastic films deposited onto structural alloys. For this purpose, it is surmised that the film is too thin to have any effect on the strains, except through its influence on the static friction coefficient. The approach has been demonstrated in a companion paper for thin diamond-like carbon films deposited onto steel substrates (Wang et al., 1998). This sphere impression method uses the strain at film cracking to characterize its toughness. It may also be used to assess the adhesion.

In another aspect of the study, indentation stress/strain curves have been calculated and related to the uniaxial stress/strain behavior of the material. It is found that, upon using a strain definition proposed by Johnson (1970), there is an explicit relation independent of the yield strain and the elastic modulus for each strain hardening exponent. This finding extends previous correlations which had been restricted to the fully plastic limit. These functions are useful for determining the plastic properties of the substrate from the indentation load/displacement curve, as elaborated in the companion paper (Wang et al., 1998).

Acknowledgements

The work was supported in part by the NSF through the Harvard's MRSEC grant, in part by the ONR grant, N00014-96-1-0059 and in part by the Division of Engineering and Applied Sciences, Harvard University.

References

Bentzon, M.M., Barholmhansen, C., Hansen, J. B., 1995. Diamond and Related Materials 4, 787–790.
Bhattacharya, A.G., Nix, W.D., 1991. Int. J. Solids Structures 27, 1058.
Biwa, S., Storåkers, B., 1995. J. Mech. Phys. Solids 43, 1303.
Blanpain, B., Celis, J. P., Roos, J. R., Ebberink, J., Smeets, J., 1993. Thin Solid Films 223, 65–71.
Briscoe, B.J., Sebastian, K.S., Adams, M.J., 1994. J. Physics D 27 1156–1162.
Bull, S.J., 1995. Diamond and Related Materials 4, 827–936.
Bull, S.J., Chaiker, P.R., 1995. Journal of Metals 47, 16–19.
Deng, J.G., Braun, M., 1995. Diamond and Related Materials 4, 936–947.
Fischer-Cripps, A.C., Lawn, B.R., 1996. J. Am. Ceram. Soc. 79, 2609–2618.
Grill, A., Patel, V., 1993. Diamond and Related materials 2, 597–605.
Hill, R., Storåkers, B., Zdunek, A.B., 1989. Proc. R. Soc. Lond. A 423, 301–330.
Johnson, K.L., 1970. J. Mech. Phys. Solids 18, 115–126.
Johnson, K.L., 1985. Contact Mechanics. Cambridge University Press, Cambridge, U.K.
Komvopoulos, K., 1989. J. Tribology 111, 430–439.
Kral, E.R., Komvopoulos, E.R., Bogy, D.B., 1993. J. App. Mech. 60, 829–841.
Kral, E.R., Komvopoulos, E.R., Bogy, D.B., 1995a. J. App. Mech. 62, 20–28.
Kral, E.R., Komvopoulos, E.R., Bogy, D.B., 1995b. J. App. Mech. 62, 29–42.

Meletis, E.I., Erdemir, A., Fenske, G.R., 1995. Surface and Coating Technology 73, 39–45.
Pharr, G.M., Oliver, W.C., Brotzen, F.R., 1994. J. Mater. Res. 7, 613–617.
Storåkers, B., Biwa, S., Larsson, P.-L., 1997. Int. J. Solids and Structures 34, 3061–3083.
Wang, J.S., Sugimura, Y., Evans, A.G., Tredway, W., 1998. Thin Solid Film 325, 163–174.
Wei, R., Wilbur, P.J., Kustas, F.M., 1992. J. Tribology, Trans. ASME 114, 298–303.
Weppelman, E., Swain, M.V., 1996. Thin Solid Films 286, 111–121.
Wuttiphan, S., Pajares, A., Lawn, B.R., Berndt, C.C., 1997. Thin Solid Films 293, 251–260.